Journal of Applied Fluid Mechanics, Vol. 17, No. 2, pp. 370-383, 2024.
Available online at www.jafmonline.net, ISSN 1735-3572, EISSN 1735-3645.
https://doi.org/10.47176/jafm.17.02.2081

Application of Wavenumber-frequency Method for Characteristic Frequency Prediction of Cavity Noise at Subsonic Speeds

W. Lu [1], L. Wei [1, 2], Y. Wang [1, 3], G. Yang [1, 2], G. Zheng [1, 3, †] and Z. Sun [1, 3]

[1] *Institute of Mechanics, Chinese Academy of Sciences, Beijing, 100190, China*
[2] *School of Future Technology, University of Chinese Academy of Sciences, Beijing, 100049, China*
[3] *School of Engineering Science, University of Chinese Academy of Sciences, Beijing, 100049, China*

†*Corresponding Author Email: zhengguannan@imech.ac.cn*

ABSTRACT

Flow-acoustic feedback is one of the main types of noise in a cavity, is caused by the instability of the cavity shear layer and is enhanced through an acoustic-wave feedback mechanism. The flow characteristics of the cavity boundary/shear layer and the characteristic frequencies of the flow-acoustic feedback in the cavities are studied numerically, with aspect ratios ranging from 1/2 to 4/3. The freestream Mach number is equal to 0.11, corresponding to an Re-based cavity length of 2.1×10^5. Improved Delayed Detached Eddy Simulations combined with Ffowcs Williams-Hawkings acoustic analogy are used to simulate the flow and noise characteristics of the cavities. Auto-correlation analysis of flow field fluctuations is used to establish a link between the boundary/shear layer pressure fluctuations and flow-acoustic feedback noise. For the low aspect ratio cavities investigated in this paper, convection velocities along the shear layer development direction are obtained using wavenumber-frequency analysis. The deeper the cavity, the lower the shear layer flow velocity. Correspondingly, the characteristic frequencies of the narrowband noise generated by the flow-acoustic feedback shift linearly toward the low frequency band as the cavity depth increases. The results of the predicted noise characteristic frequencies obtained using wavenumber-frequency analysis and Rossiter's empirical formula are in agreement with the calculated results.

Article History

Received June 12, 2023
Revised July 26, 2023
Accepted September 28, 2023
Available online December 4, 2023

Keywords:

Cavity noise
Flow-acoustic feedback
Wavenumber-frequency analysis
Pressure fluctuation
Flow instability

1. INTRODUCTION

Uncovered cavities are prevalent within airframes, encompassing landing gear bays (Moreau, 2022; Zhang et al., 2022), landing gear hubs (Casalino et al., 2014; Zhao et al., 2020), and high-lift coves (Chen et al., 2021; Vadsola et al., 2021). All of these can be considered as integral cavity components on aircraft. The resonances emitted from these cavities become entwined with the noise generated by blunt body components, culminating in a more complex soundscape that causes passenger unease (Delcor et al., 2022) and directly determines the noise level during take-off and landing (Dobrzynski, 2010). Hence, the predicament of flow-induced cavity noise has long remained a focal point of scholarly inquiry and a central concern within the engineering community (Guo et al., 2022). Flow-induced noise within cavities can be classified into three distinct categories based on their underlying causes: flow-acoustic feedback noise, acoustic resonance noise, and fluid-elastic interaction noise (Rockwell & Naudascher 1978). Flow-acoustic feedback and acoustic resonance are the two primary origins of self-sustained oscillation noise induced by the flow within rigid-wall cavities.

Roshko (1955) stands as the pioneer who embarked upon experimental measurement and analysis of cavity flow, setting the stage for subsequent investigations into cavity research (Gharib & Roshko, 1987). Following in his footsteps, numerous scholars have delved into the intricacies of flow-acoustic feedback phenomena within cavities, unraveling the mechanisms behind noise generation and discovering a plethora of semi-empirical relationships that align with experimental observations (Powell, 1961). Among these relationships, the Rossiter formula (Rossiter, 1964) reigns supreme, being widely embraced and employed. Assuming constant vortex velocity and equivalence of sound speed both within and outside the cavity, Rossiter devised a semi-empirical

NOMENCLATURE

PSD	Power Spectral Density	f	frequency
U_v	convection velocity	U_∞	incoming flow velocity
U	velocity	α	phase delay coefficient
κ	ratio of turbulent motion velocity to incoming flow velocity	ω	angular frequency
k	wave number	Ma	Mach number

formulation to anticipate characteristic frequencies while introducing two empirical parameters: α (phase delay coefficient) and κ (ratio of turbulent motion velocity to incoming flow velocity).

The depth of a cavity exerts a discernible influence on the values of α and κ. α has a range of values, and for shallow cavities, Rossiter (1964) empirically fine-tuned the value of α to align with his experimental data. These adjusted values are conveniently compiled in a tabular format for shallow cavities with aspect ratios (L/D) ranging from 1 to 10. Conversely, Larcheveque et al. (2003) used on large-eddy simulations (LES) to investigate the flow dynamics over deep cavities. Their findings led to the proposal of novel empirical values for the phase delay coefficient α within Rossiter's model, particularly catering to deep cavities and considering a fixed Strouhal number mode. Similarly, κ also has a range of values, intricately linked not only to the aspect ratios of the cavity but also to the flow characteristics of the turbulent boundary/shear layer near the cavity opening. At transonic and supersonic speeds, Heller et al. (1971) introduced a ratio of flow velocity to local sound velocity M_c as an additional adjustment to κ, forming the well-known Rossiter-Heller formula. East (1996) conducted experimental investigations into the flow characteristics surrounding rectangular cavities with large aspect ratios, enabling the measurement of κ values within the range of 0.35 to 0.6. Building upon this research, Ma et al. (2009) delved into the flow-induced feedback of the same rectangular cavities and concluded that the κ range was narrower than that observed by East, spanning from 0.22 to 0.43. Furthermore, DeChant (2019) derived a specialized Rossiter-style model, sensitive to cavity depth, for shallow cavities with aspect ratios exceeding 1. This model aimed to estimate shear-cavity tones and, while approximate in nature, its analytical foundation solidifies the physical basis that underlies all expressions of Rossiter-style cavity modes. Casalino et al. (2022) further revised the value of κ in the Rossiter-Heller formula for rectangular cavities in subsonic and supersonic flow conditions (Ma>0.6).

The determination of κ is paramount in anticipating the characteristic frequencies of flow-acoustic feedback noise, prompting extensive research in this field, predominantly through experimental means. While wind tunnel tests yield precise κ measurements; however, they pose challenges due to the wide array of cavity shapes, the arduous production of experimental samples, and the associated high costs. However, with the rapid advancements in computer technology, numerical simulation methods have emerged as not only reliable but also cost-effective alternatives to experimental methods. Ji & Wang (2012) embarked on a numerical exploration of the intricate flow characteristics surrounding three-dimensional forward and backward steps, unraveling the mechanisms underlying the generation of pressure sources in these configurations. Comte et al. (2008) studied the passive control of cavity flow instability using the LES method, effectively validating the reliability of numerical simulations by comparing them with experimental data. Employing an implicit approach, Li et al. (2013) investigated the interplay between vortex shedding and acoustic excitation within a rectangular cavity, conclusively affirming that flow-acoustic feedback constitutes the principal driving force behind the self-sustained oscillation observed in the studied cavity. Furthermore, Ahuja & Mendoza (1995) utilized the FW-H (Ffowcs Williams-Hawkings) equation to calculate the far-field characteristics and directivity of cavity noise. Ashcroft & Zhang (2001) computationally explored the noise radiated by flow-induced cavity oscillations, employing the URANS (Unsteady Reynolds-Averaged Navier-Stokes) method and the FW-H equation. Remarkably, their computed Rossiter modes exhibited an excellent agreement with the reported experimental values.

Nevertheless, there exists a scarcity of research concerning cavities characterized by small aspect ratios. Dalmont et al. (2001) presented compelling findings indicating that flow-acoustic feedback noise is the prevailing mechanism for cavities with aspect ratios below 1. These results were further substantiated by the experimental findings of Guo et al. (2021), validating Dalmont's assertion that significant flow-acoustic feedback noise in cavities posseses an aspect ratio of 2/3.

Thus, we conducted a comprehensive numerical investigation into the flow characteristics of a boundary/shear layer near cavity mouths, as well as the flow-acoustic feedback noise characteristics within cavities of different depths at a Mach number of 0.16. The primary aim is to elucidate the influence of cavity depth on the characteristic frequency of the flow-acoustic feedback noise and to provide accurate predictions of this frequency using the wavenumber-frequency method and Rossiter's empirical formula. The paper is structured as follows: Section 2 provides a detailed description of the numerical simulation setups, encompassing the simulation models, computational methodologies, and verification of the numerical simulations. Section 3 outlines the analytical methods employed, including Rossiter's empirical formula and the wavenumber-frequency spectral analysis technique. In Section 4, the obtained results are discussed. Finally, Section 5 summarizes the conclusions drawn from the study.

2. NUMERICAL SETUP

2.1 Computational Models

The computational model used in present study is a cavity model with infinite spanwise, that is, the cavity width $W = \infty$ as shown in Fig. 1. The influence of spanwise on cavity flow can be disregarded. Similarly, in terms of cavity noise, the frequencies associated with the width and depth modes are considered infinitesimal, as per the prediction formulas for acoustic resonant tones proposed by Ahuja & Mendoza (1995) and Dalmont et al. (2001).

To facilitate verification of the reliability of the simulation method, the cavity length (L) for the Base case measures 0.08 m, while its depth (D) is 0.12 m. These dimensions adhere to the aspect ratio specifications outlined by Guo (2020), and Gue et al. (2021). The other cavity depths used are 0.06 m, 0.08 m, 0.1 m, 0.14 m, and 0.16 m, which correspond to aspect ratios of 4/3, 1, 4/5, 2/3, 4/7, and 1/2, respectively, as presented in Table 1. The distance from the front edge of the cavity to the inlet measures 0.2 m.

An array for monitoring turbulent pressure fluctuations is positioned at 0.01 L above the cavity mouth's centerline and the rear wall of the cavity. Its purpose is to capture the wavenumber-frequency characteristics of pressure fluctuations within the boundary/shear layer in the proximity of the cavity mouth. The array is illustrated by the red dots in Fig. 1. The virtual pressure monitoring array is composed of 300 points in the x-direction, with a spacing of 0.01 m between each point.

To examine the sound pressure characteristics associated with the cavity noise, two pressure measurement points are strategically located. The first point is positioned on the centerline of the cavity bottom, while the second point is placed at a distance of 5L above the centerline of the cavity mouth's front edge. These specific locations are indicated by the red solid points in Fig. 1.

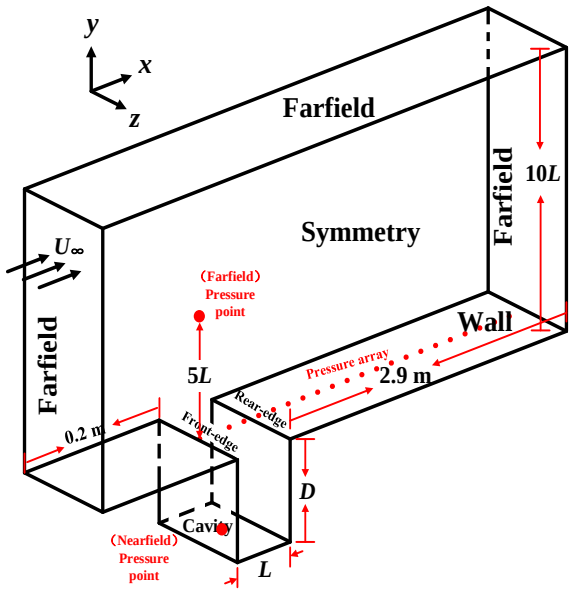

Fig. 1 Schematic diagram of computational domain

Table 1 Geometrical parameters of cavities in this paper

	Length [mm]	Depth [mm]	L/D
Case1	80	60	4/3
Case2	80	80	1
Case3	80	100	4/5
Base case	80	120	2/3
Case4	80	140	4/7
Case5	80	160	1/2

Table 2 Details of the computational grids

	$N_x \times N_y \times N_z$	Quantity (Million)	First cell height
Coarse	260×80×100	2.1	$2\times10^{-3}L$
Medium	340×100×120	4.1	$1\times10^{-3}L$
Fine	400×120×160	7.7	$5\times10^{-4}L$

2.2 Computational Algorithms

In this study, a three-dimensional grid is constructed using ANSYS ICEM, a mesh generation software. The computational domain chosen for investigation is illustrated in Fig. 1, with dimensions of $L \times W \times H$= 3180 mm × 240 mm × 800 mm. Three distinct mesh types are employed, categorized as coarse, medium, and fine, with various grid densities. Specifically, the total number of cells for the respective meshes is 2.1 million, 4.1 million, and 7.7 million, as presented in Table 2, which provides a comprehensive breakdown of the details pertaining to these three computational grids.

The computational fluid dynamics software FLUENT is used as the numerical solver. The gas properties are set as those of an ideal-gas. The inlet and outlet of and the location above the computational domain are all set as the pressure-far-field, and the two sides of the computational domain are symmetrical. The temperature and pressure are consistent with the experimental environment of the work of Guo et al. (2021): T_∞ = 303 K and P_∞ = 101325 Pa. The cavity and the bottom of the computational domain are no-slip walls, as shown in Fig. 1.

First, the steady k-ε two-equation model is used to simulate a turbulent flow field. Pressure-velocity coupling is dealt with by using the SIMPLEC algorithm. The pressure, density, momentum, and turbulent kinetic energy in the equation are two-order upwind schemes. The improved delayed detached eddy simulation method is used to calculate the transient flow field to obtain the acoustic sources, and an FW-H acoustic analogy is employed to calculate the acoustic field. The initial time step $\Delta t = 1 \times 10^{-5}$ s. After obtaining converged flow field information, the time step is increased to 5×10^{-5} s. The total calculation time for the flow field is 1.2 s, and the time for the acoustic field is 1 s. The convergence criterion is that the residuals of the continual terms are less than 10^{-5}.

The Improved Delayed Detached Eddy Simulation (IDDES) method originates from the Detached Eddy Simulation (DES) proposed by Spalart (1997). DES

combines Large Eddy Simulation (LES) with the Spalart-Allmaras (SA) model. It automatically transitions between the two models by comparing the local grid scale and wall distance. Spalart et al. (2006) further developed the Delayed Detached Eddy Simulation (DDES) by introducing a "Delay LES function" based on Menter's SST model (Menter, 1994). DDES employs the delay function to mitigate mesh-induced separation issues in the original DES, but it can lead to a phenomenon known as log-layer mismatch (LLM). LLM refers to the mismatch between vortex viscosity coefficient distribution and velocity characteristics between Reynolds-Averaged Navier-Stokes (RANS) and LES in the logarithmic region. To address this, Shur et al. (2008) proposed the IDDES, which incorporates a lifting function to suppress LLM. Additionally, IDDES introduces a branch of Wall-Modeled LES (WMLES). When the boundary layer grid is sparsely resolved, IDDES behaves similarly to DDES. However, when the boundary layer grid is densely resolved, IDDES automatically transitions to WMLES. This feature of IDDES significantly expands its applicability in engineering contexts.

The FW-H model (The Ffowcs-Williams and Hawkings Model) is essentially a fluctuation equation, which can be derived from the continuity equation and the Navier-Stokes equation. The FW-H model (Ffowcs-Williams & Hawkings, 1969) can be expressed in the following form:

$$\frac{1}{a_0^2}\frac{\partial^2 p'}{\partial t^2} - \nabla^2 p' = \frac{\partial^2}{\partial x_i \partial x_j}\{T_{ij}H(f)\} - \frac{\partial}{\partial x_i}\{[P_{ij}n_j + \rho u_i(u_n - v_n)]\delta(f)\} + \frac{\partial}{\partial t}\{[\rho_0 v_n + \rho(u_n - v_n)]\delta(f)\} \quad (1)$$

Where u_i is the component of the velocity of the fluid in the x_i direction. u_n is the component of fluid velocity in the normal direction of the wall; v_i is the component of the surface velocity in the x_i direction. v_n is the component of surface velocity along its normal direction; $\delta(f)$ is the Dirac function. $H(f)$ is the Heavyside's unit function.

p' is the far-field sound pressure. f =0 represents a mathematical surface embedded in the unbounded space of the external flow problem (f > 0), so that it can be solved easily using generalized function theory and free space Green's function.

a_0 is the far-field sound speed, and T_{ij} is the Lighthill stress tensor, defined as:

$$T_{ij} = \rho u_i u_j + P_{ij} - a_0^2(\rho - \rho_0)\delta_{ij} \quad (2)$$

P_{ij} is the compressive stress tensor. For Stokesian fluids, the compressive stress tensor is given by:

$$P_{ij} = p\delta_{ij} - \mu[\frac{\partial u_i}{\partial x_j} + \frac{\partial u_j}{\partial x_i} - \frac{2}{3}\frac{\partial u_k}{\partial x_k}\delta_{ij}] \quad (3)$$

2.3 Numerical Validation

In situations where the aspect ratio is below 1, the free shear layer located above the cavity mouth predominantly exhibits two-dimensional behavior, featuring tightly coherent rolls in the spanwise direction. The length-to-depth ratio of the cavity model is set at 1/3, aligning with the flow characteristics typically observed in two-dimensional cavity flows. Consequently, the mesh and simulation methodology adopted in this study are validated through a comparative analysis using the experimental data from the work of Guo (2020), and Gue et al. (2021).

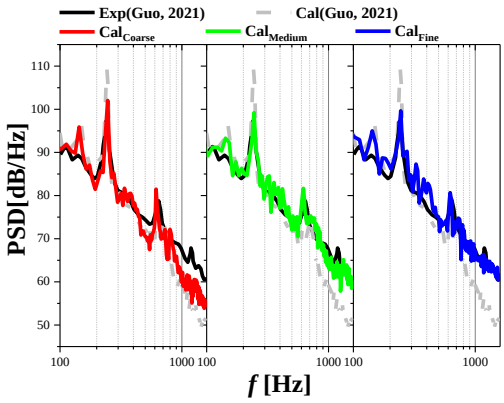

Fig. 2 Acoustic field information verification results at the Mach numbers of 0.16

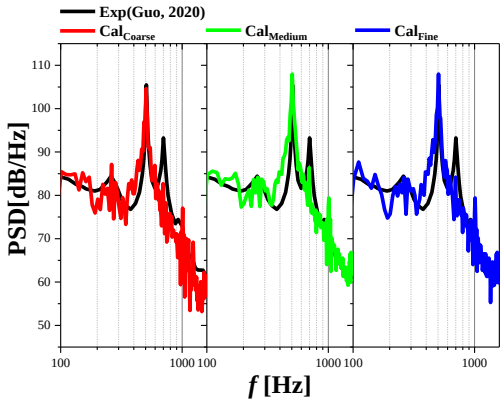

Fig. 3 Acoustic field information verification results at the Mach numbers of 0.11

Numerical verification of the acoustic field is performed for the Base case at Ma numbers of 0.11 and 0.16. Fig. **2** and Fig. 3 show the power spectral density of the near-field noise calculated using the three computational grids. In Fig. 2, the black solid line represents the experimental results from the study of Guo et al. (2021), while the grey dashed line corresponds to the calculations performed by Guo et al. (2021). The red, green, and blue lines represent the results obtained from the three grids respectively. A comparison with the experimental data shows that the coarse mesh resolution produces significant calculation errors in the high-frequency range. However, as the resolution increases from coarse to medium and then fine, the numerical simulation results for the broadband noise intensity align closely with the experimental findings. Furthermore, Fig. 2 shows the presence of several narrowband noises superimposed on the broadband spectrum in the experimental results. The dominant tone is characterized by a frequency of 244 Hz. Notably, all numerical simulation results effectively reproduce the frequencies associated with these narrowband noises, with errors in the intensity of the dominant tone remaining below 3%.

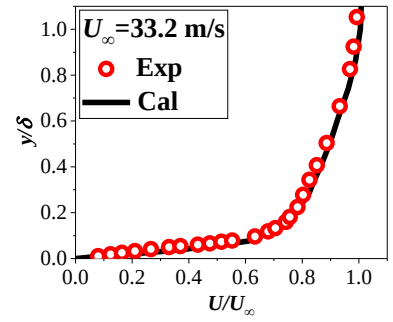

(a)

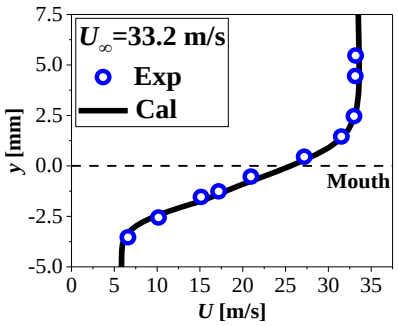

(b)

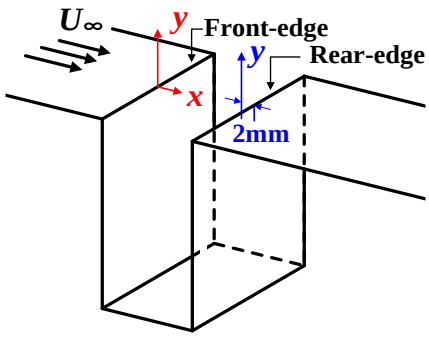

(c)

Fig. 4 Flow field information verification results for an incoming flow velocity of 33.2 m/s. (a): Time-averaged velocity profile of the boundary layer at the front edge of the cavity mouth. (b): Time-averaged velocity profile of the shear layer at 2 mm upstream of the rear-edge of the cavity mouth. (c): Schematic diagram of selected locations of the boundary layer and shear layer

Fig. **3** shows the comparison results when the Ma number is 0.11. The numerical simulation results calculated by the medium grid are almost agree with those calculated by the fine grid. Referring to the experimental results (Guo, 2020), the broadband amplitude and dominant frequency amplitude are basically consistent with the experimental values, with an error of less than 3%.

According to the analysis above, the results obtained using medium grid resolution show minimal discrepancies compared with those obtained using fine grid resolution. To optimize computational accuracy and because of limited computing resources, the subsequent numerical verifications and calculations are performed using grid resolutions that match those of the medium grid.

According to the analysis above, there is little error between the results for medium and fine grid resolution. Therefore, to maximize calculation accuracy and minimize computing resources, the grids in subsequent numerical calculations are generated using the medium grid.

Flow field verifications are conducted with an incoming flow velocity of U_∞=33.2 m/s, corresponding to an Ma number of 0.095. Fig. 4 (a) and Fig. 4 (b) show the time-averaged velocity profiles of the boundary layer at the front-edge and the shear layer at 2 mm upstream of the rear-edge, respectively. Fig. 4 (c) shows the selected locations for the boundary layer and shear layer. The time-averaged velocity profiles are obtained by averaging 100 instantaneous velocity profiles with a time interval of 0.0001 s. Fig. 4 (a) and Fig. 4 (b) show that the results of the time-averaged velocity profile obtained in the numerical simulation agree well with the experimental results. In Fig. 4 (a), the slopes of the flow velocity profile within and outside the boundary layer exhibit good agreement with the experimental findings. Likewise, in Fig. 4 (b), the span of the shear layer at the upstream position and the flow velocity profile within the shear layer obtained from the simulation results are in substantial agreement with the experimental results (Guo, 2020).

Therefore, based on the strong agreement between the numerical results and experimental data, we conclude that the computational methods and calculation grid employed in this study are reliable.

The numerical simulations of cavities with different depths conducted in this paper are performed under an incoming flow velocity of U_∞=38.38 m/s, corresponding to an *Ma* number of 0.11.

3. ANALYTICAL METHODS

3.1 Rossiter Formula

Based on the principle of the flow-acoustic feedback of a cavity, Rossiter (1964) was the first to propose a formula for predicting the characteristic frequency of the cavity noise:

$$St = \frac{f \cdot L}{U_\infty} = \frac{n-\alpha}{1/\kappa + Ma} \tag{4}$$

where $n = 1,2,$, is the mode number of the self-oscillation noise. κ is a semi-empirical constant, which can be regarded as the ratio of the convection velocity U_v to the incoming flow velocity U_∞. For $\boldsymbol{L/D}$ >4, the prediction results in Eq. (4) are in the agreement with the experimental data when κ=0.57. α is another empirical constant, which can be regarded as the delay factor between the time a vortex reaches the rear-edge and the new acoustic wave radiation generates. For shallow cavities with $\boldsymbol{L/D}$ between 1 and 4, α is equal to 0.25.

Based on Eq. (4), Larcheveque et al. (2003) found that the evaluation of α is very sensitive to the value of κ. They introduced new values in accordance with $\boldsymbol{L/D}$ for α

constant into Rossiter's formula and proposed new low values for low aspect ratios; the data are fitted using the empirical equation:

$$\alpha = 0.58e^{-((L/D-10)/6)^2} \quad (5)$$

The trend in α predicted by Eq. (5) is in good agreement with Rossiter's experiments, Forestier's (2000) experiments, and Larcheveque's own calculations.

3.2 Wavenumber-Frequency Spectrum Analysis

The wavenumber-frequency spectral analysis method represents a novel approach within the realm of wave analysis. This method primarily involves the transformation of signals from the space-time domain to the wavenumber-frequency domain. Through an analysis of the wavenumber-frequency spectrum, wave propagation information can be derived (Tang & Rockwell 1983).

By employing a two-dimensional Fourier transform of the space-time surface pressure, the wavenumber-frequency information of surface pressure fluctuations can be obtained. This information reveals the magnitude distribution of specific wave components in the wavenumber-frequency domain, providing insights into the propagation velocity and direction of the waves (Arguillat et al., 2005).

The two-dimensional Fourier expression is:

$$F(K,\omega) = \int_{-\infty}^{+\infty}\int_{-\infty}^{+\infty} f(x,t)e^{-i(Kx+\omega t)}dxdt \quad (6)$$

where K is the wave number, and ω is the angular frequency ($\omega = 2\pi f$ and has unit of rad/s). Due to the limited space and time of measurement, a discrete two-dimensional Fourier transform is generally performed on the discrete space-time signal of the pulsating pressure, and its expression is:

$$P(K,\omega) = \frac{2\left|\sum_{n=1}^{N}\sum_{m=1}^{M} W(x_m,t_n)p(x_m,t_n)e^{-i(K_x x_m+\omega t_n)}\right|}{MN} \quad (7)$$

where M is the number of time nodes, N is the number of monitoring points of the space pulsating pressure, $W(x_m)$ and $W(t_n)$ are both window functions (the Hanning window is used in this paper), and p is the pulsating pressure of the monitoring point, in Pa. The discrete two-dimensional Fourier transform has corresponding restrictions on the frequency and wavenumber intervals of the transformation. The frequency limit F_{max} is half the inverse of the sample time distance $\mathrm{d}T$; that is, $F_{max} = 0.5/\mathrm{d}T$. The wavenumber limit K_{max} is half the inverse of the sampling point spacing $\mathrm{d}X$; that is, $K_{max} = 0.5/\mathrm{d}X$.

Due to the contrasting propagation velocities of fluid waves and acoustic waves, the flow convection velocity (U_v) is significantly smaller than the sound speed (c). Consequently, the convection wavenumber ($k_v = 2\pi f/U_v$) is much larger than the acoustic wavenumber ($k_c = 2\pi f/\mathrm{c}$). The wavenumber-frequency spectral method enables the decomposition of the surface pressure into distinct flow components and acoustic components, identifiable by the distinct peaks on a wavenumber-frequency spectral diagram, as depicted in Fig. 5.

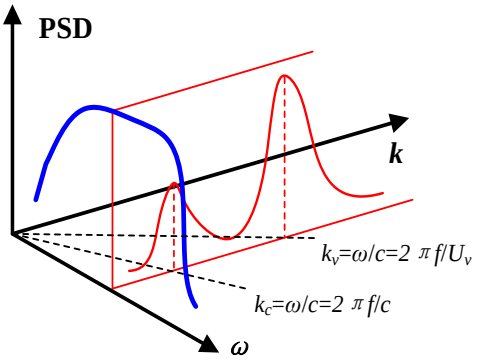

Fig. 5 Wavenumber-frequency (k-ω) diagram for wall pressure fluctuations of a subsonic flow (Bremner & Zhu 2003)

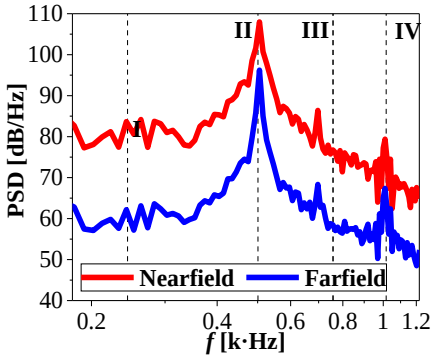

Fig. 6 Comparison results of the numerical simulation and empirical prediction of characteristic frequencies of flow-acoustic feedback noise of Base case at the Ma=0.11

4. RESULTS AND DISCUSSIONS

4.1 Spectral Characteristics of Cavity Noise

Fig. 6 shows both the numerical simulation results and the predictions obtained using Rossiter's empirical formula, incorporating a new value of α based on $\boldsymbol{L/D}$. The characteristic frequencies estimated using the empirical formula are represented by black dashed lines, with I, II, III, and IV denoting the 1st, 2nd, 3rd, and 4th modes of the flow-acoustic feedback, respectively. The red line corresponds to the simulation result of the near-field, while the blue line corresponds to the simulation result of the far field.

In Fig. 6, the near-field noise spectrum of the Base case exhibits multiple distinct narrowband peaks with various intensities, indicating cavity oscillation. The dominant peak occurs at a frequency of 0.5 kHz. The amplitudes of both the narrowband and broadband noise in the far field are significantly attenuated when compared to the amplitude of the near-field noise, with similar levels of reduction. This suggests that cavity noise is capable of propagating into the far field.

Furthermore, the frequencies corresponding to the narrowband noise in the near and far fields remain consistent. With the exception of the 3rd peak, the

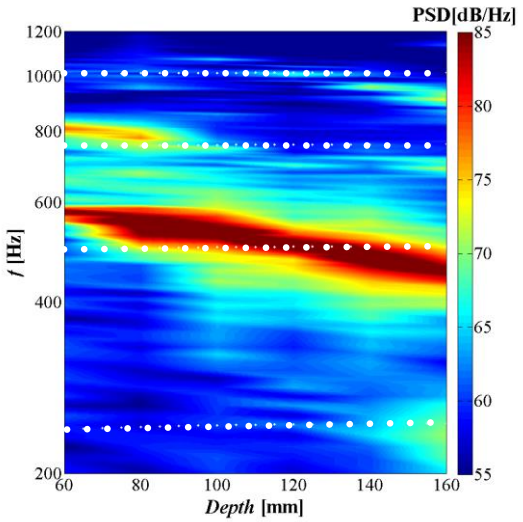

Fig. 7 Contours of power spectral density of the flow-acoustic feedback noise for different depth cavities

simulation results closely align with the prediction results. This implies that these narrowband noises indeed originate from flow-acoustic feedback.

Fig. 7 shows numerical simulation results of the power spectral density for the flow-acoustic feedback noise in cavities of varying depth, as investigated in this study. The white dotted lines represent the predictions obtained using the empirical formula, employing $\alpha = 0.58e^{-((L/D-10)/6)^2}$ and κ = 0.57. Similar to the Base case, cavities with different depths exhibit distinct narrowband noises superimposed on the low to mid-frequency broadband noise, corresponding to various modes of the flow-acoustic feedback phenomenon. It is worth noting that the characteristic frequencies associated with the modes of acoustic feedback noise in the cavities with different depths are not consistent. As cavity depth increases, the frequencies shift toward the low-frequency range. Furthermore, there is a discrepancy between the predicted and calculated results, which confirms the previous understanding that κ represents a range value.

In addition, the noise amplitude of the 2nd mode is the largest of all the cases under investigation in this paper. Cavity depth has almost no effect on the broadband amplitude of the cavity noise.

Table 3 provides simulation results for the characteristic frequencies corresponding to flow-acoustic feedback noise. Consistent with the findings depicted in Fig. 7, the frequencies associated with the flow-acoustic feedback noise for each mode, except the 3rd mode of the Base case, follow a trend of linearly shifting toward the low-frequency range as cavity depth increases.

Previous studies (East, 1966; Ma et al., 2009) on the convection characteristics of large aspect ratio cavities (L/D>1) have suggested a range for κ, of 0.22 to 0.6. Fig. 8 compares the calculated and predicted results for the characteristic frequencies of the flow-acoustic feedback noise, with the dotted and dashed lines representing κ values of 0.22 and 0.6, respectively. When κ is 0.22, the predicted characteristic frequencies are

Table 3 Frequencies corresponding to flow-acoustic feedback noise

f_n [Hz]	$n = 1$	$n = 2$	$n = 3$	$n = 4$
Case1	394	576	808	--
Case2	354	556	778	--
Case3	323	535	747	1071
Base case	263	505	697	1010
Case4	232	475	717	960
Case5	232	455	687	909

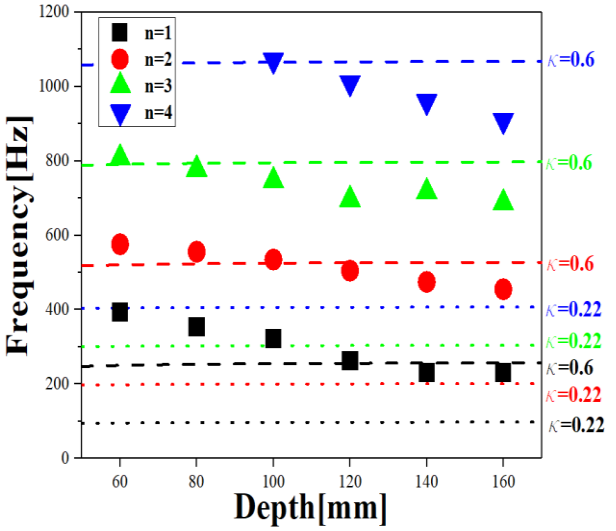

Fig. 8 Comparison of the calculated and predicted results for the characteristic frequencies of flow-acoustic feedback noise (dotted and dashed lines correspond to κ values of 0.22 and 0.6, respectively)

significantly lower than the calculated results. Conversely, when κ is 0.6, the predicted results align closely with the calculated results for cavity depths of 0.1 m and 0.12 m. This indicates that for the small aspect ratio cavities investigated in this study, κ is approximately 0.6, and should be regarded as a range value.

4.2 Analysis of Shear Layer Convective Characteristics

According to the definition of the Rossiter prediction model, κ is the ratio of the convection velocity U_v to the incoming flow velocity U_∞. In order to clarify the value of κ, this subsection focuses on the convective characteristics of the shear layer near the cavity mouth.

Figure 9 shows contour maps of the time-averaged velocity in all cavities. Across cavities with various depths, the time-averaged velocity gradually increases along the incoming flow direction near the cavity mouth until the vicinity of the rear-edge of the cavity mouth, where it decreases. The contour maps clearly show that the velocity distributions are essentially the same near the cavity mouth and outside the cavity, with variations primarily occurring within the recirculation zone inside the cavity. Notably, the time-averaged velocity within the recirculation zone is largest in the square cavity (Case 2). As the cavity aspect ratio increases, the area of the

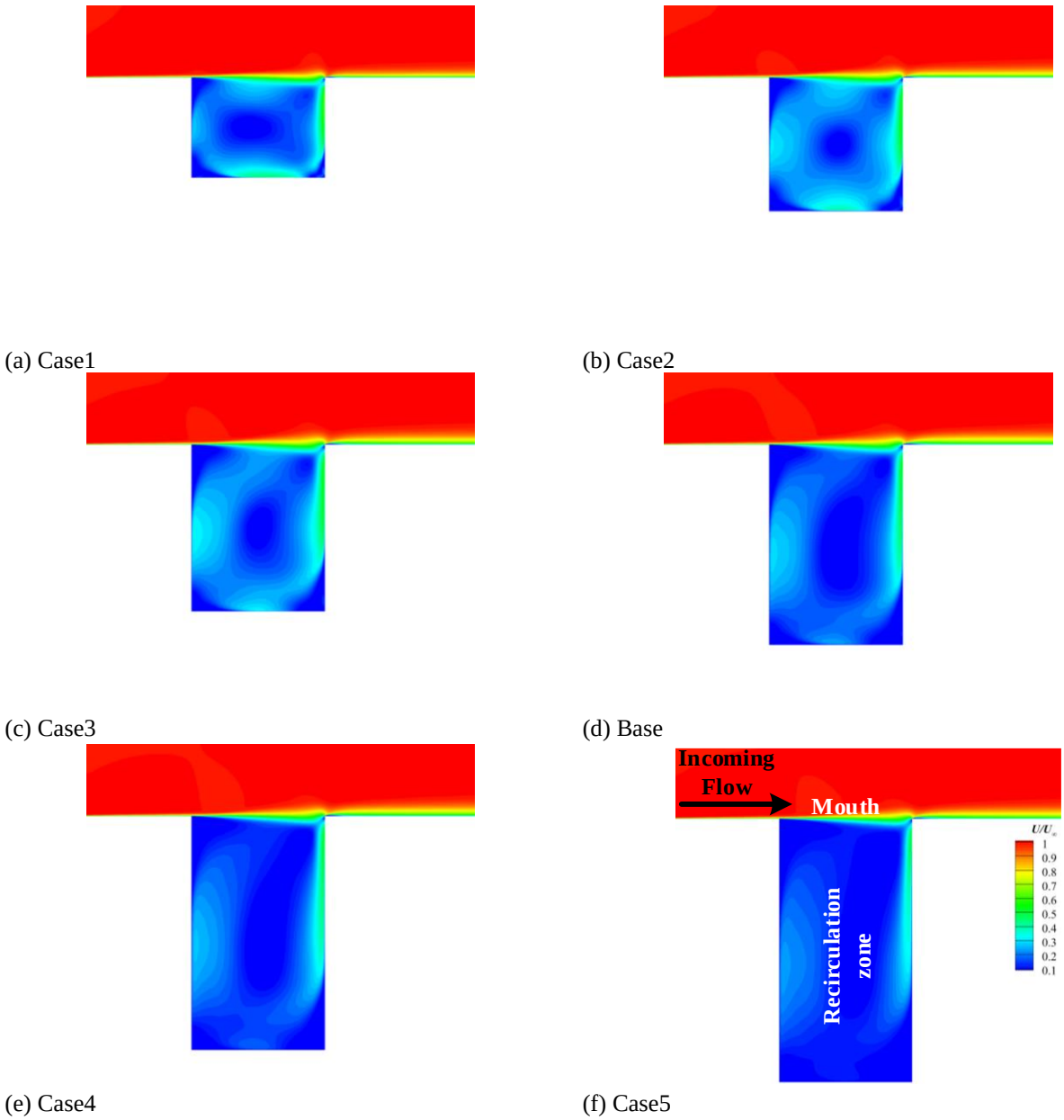

Fig. 9 Contour maps of time-averaged velocity for all cavities

recirculation zone increases, while the time-averaged velocity decreases.

Figure 10 shows the time-averaged velocity profiles of the boundary layer and shear layer at different locations on the cavity mouth. The red, orange, yellow, green, blue, and purple lines correspond to the time-averaged velocity results for cavity depths of 0.06 m, 0.08 m, 0.1 m, 0.14 m, and 0.16 m, respectively.

For cavities with various depths, their incoming boundary layer velocity profiles nearly overlap, indicating consistency in the incoming boundary layer velocities. Due to momentum exchange between the flow inside and outside the cavity, the time-averaged velocity increases along the incoming flow direction at the cavity mouth (Y = 0). The acceleration of the shear layer flow differs slightly among cavities of different depths, with the acceleration tendency becoming more pronounced for smaller cavity depths. Additionally, at the rear-edge of the cavity (X/L = 1), the boundary layer velocity increases as

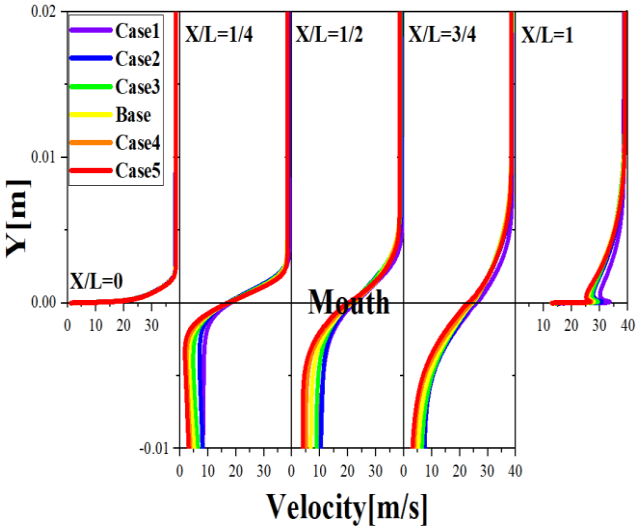

Fig. 10 Boundary/shear layer velocity distribution at different locations on the cavity mouth

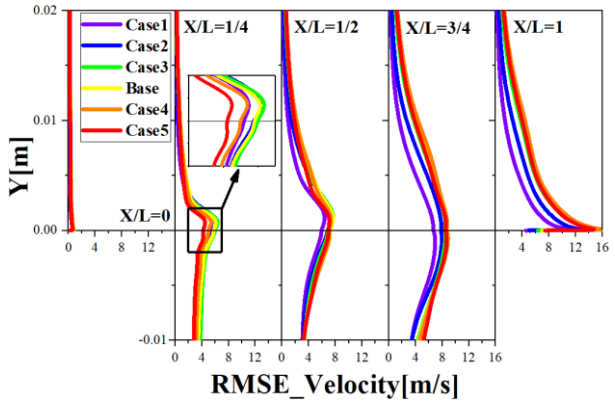

Fig. 11 RMSE of the boundary/shear layer velocity at different locations on the cavity mouth

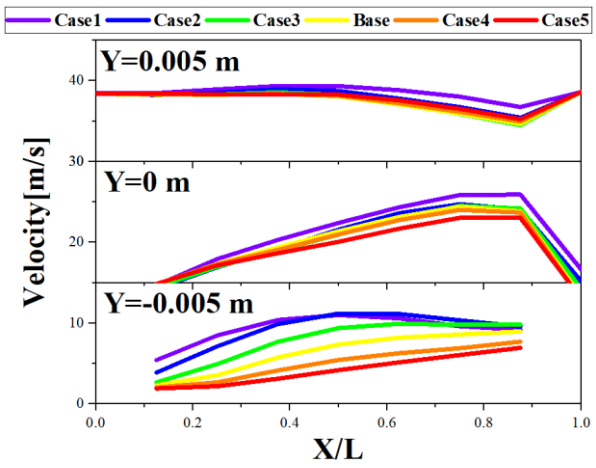

Fig. 12 Time-averaged velocity of flow for different spatial locations and cavity depths

the cavity depth decreases. Figure 10 shows that the time-averaged velocity of the shear layer flow differs for cavities with different depths. Qualitatively, a deeper cavity corresponds to a lower flow velocity. However, this analysis does not determine the specific value of κ; it only provides insight into the trend of κ as the cavity depth changes.

Figure 11 shows the root mean square error (RMSE) of the boundary layer and shear layer velocity at various locations on the cavity mouth. When comparing cavities with different depths, the velocity fluctuations within the boundary layer of the incoming flow at the front edge (X/L = 0) are essentially identical, with an RMSE of less than 1. However, the velocity fluctuation intensity increases as the flow progresses downstream along the shear layer. Near the front edge of the cavity (X/L = 1/4), the velocity fluctuation intensity increases as the cavity depth increases, except for when the cavity depth is less than 0.1 m. At a cavity depth of 0.1 m, the velocity fluctuation intensity decreases with increasing cavity depth. Near the rear-edge of the cavity (X/L = 3/4) and at the rear-edge of the cavity (X/L = 1), the velocity fluctuation intensity increases with increasing cavity depth. It is only when the cavity depth reaches 0.14 m that the velocity fluctuation intensity starts to decrease. Therefore, as the cavity depth increases, the velocity fluctuation within the shear layer experiences a more significant increase during its development.

In Fig. 12, the time-averaged velocity of the flow is shown for different spatial locations and cavity depths. At Y = −0.005 m, which represents the interior of the cavity, the red line exhibits a linear increase from the front edge to the rear-edge of the cavity. As the cavity depth decreases, the rate of increase for the yellow line transitions from a fast, linear increase to a slow, linear increase. With further decreasing cavity depth, the green line reaches a value of 10 m/s and remains constant. The blue and purple lines, on the other hand, show a deceleration around X/L = 0.5. In general, the time-averaged velocity of the flow inside the cavity decreases as the cavity depth increases.

At Y = 0 m, which represents the cavity mouth, all the curves in Fig. 12 gradually increase from the front edge of the cavity before showing a deceleration near the rear-edge. As the cavity depth increases, the acceleration decreases. Additionally, the time-averaged velocity decreases with increasing cavity depth.

At Y = 0.005 m, which is above the cavity mouth, all the curves slowly decrease from the front-edge position and then increase near the rear-edge. The variation trend of the time-averaged velocity is exactly opposite to the results observed at the cavity mouth.

In terms of the convection velocity characteristics near the cavity mouth, the results in Fig. 12 are consistent with those in Fig. 10.

According to the results in Fig. 10 to Fig. 12, both the time-averaged velocity and the velocity fluctuation of the flow near the cavity mouth increase along the development direction of the shear layer. The deeper the cavity, the more dramatic the change in velocity fluctuation, and the lower the time-averaged velocity. That is, the deeper the cavity, the smaller the value of κ for the range of cavity depths investigated in this paper.

4.3 Wavenumber-Frequency Analysis of Pressure Fluctuations

The results in the previous subsection have clarified the variation trend of κ with respect to the cavity depth. In this subsection, the wavenumber-frequency spectral method is used to determine the value of κ.

Figure 13 shows the auto-correlation of the pressure fluctuation at 0 m, 0.1 m, 0.5 m and 1 m from the centerline of the rear-edge of the cavity mouth, where $Rpp(t)$ is the auto-correlation that is calculated using the unsteady surface pressure:

$$Rpp(t) = \frac{\overline{p(t+\tau)p(t)}}{p_{PMS}^2} \tag{8}$$

where p is the pressure, p_{PMS} is the root-mean-squared pressure, and τ is the time delay.

An auto-correlation analysis of the pressure at the rear-edge of the cavity mouth for the Base case, represented by the red line in Fig. 13, reveals a slow decaying periodic behavior characterized by a Gaussian

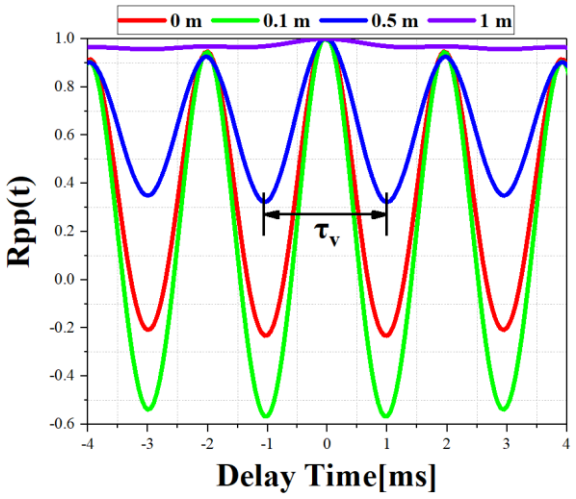

Fig. 13 Auto-correlation of the pressure fluctuation at different location

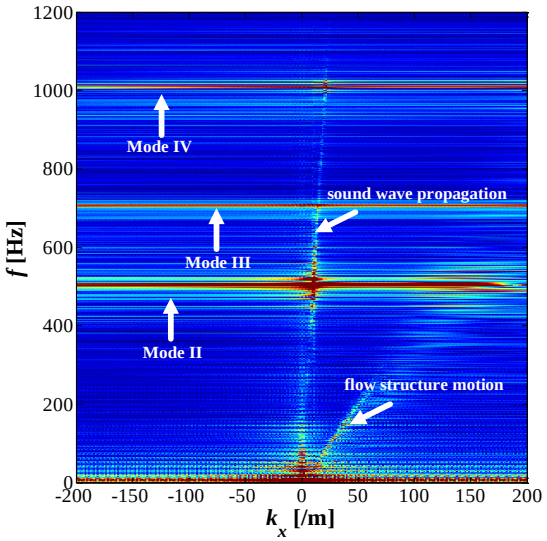

Fig. 14 Wavenumber-frequency spectral diagram of the surface pressure downstream of the cavity rear-edge (k_x: wavenumber in the x direction, f: frequency)

shape, indicating the prominent manifestation of robust flow oscillations. Notably, the flow oscillation increases markedly at a distance of 0.1 m from the rear-edge, owing to the interaction between the flow structure and the adjacent solid wall near the rear-edge. Conversely, as the pressure monitoring point progressively moves away from the rear-edge, the intensity of the flow oscillations decreases. At a distance of 1 m from the rear-edge, the oscillations become almost imperceptible. It should be noted that the intensity of the pressure oscillations varies from location to location, but the oscillations all have the same time delay, as in, τ_v. The time delay in the Base case is 0.002 s, corresponding to a frequency of 500 Hz, associated with the dominant peak in Fig. 6. These findings substantiate a robust association between the downstream flow oscillations at the cavity rear-edge and the flow-acoustic feedback noise. Moreover, the monitoring point's distance from the rear-edge point does not exert any influence on the delay time of the flow oscillations.

In Fig. 14, a wavenumber-frequency spectral diagram of the pressure fluctuation for the Base case is presented for a Mach number of 0.11. Five prominent peaks are observed in the spectrum. Three peaks exhibit a slope of 0, indicating their association with the characteristic frequencies of the principal modes. This can be attributed to the excitation of flow instabilities near the characteristic frequencies of the mode noise by acoustic-wave propagation. The fourth peak arises from the interaction between the flow and the rear-edge surface, giving rise to a distinct motion pattern within the flow structure. The fifth peak corresponds to the propagation of acoustic waves.

The slope of the peak corresponding to fluid wave propagation is 3.48 (that is, $f = 3.48 \cdot k_x$), as shown by the solid line in Fig. 14. Using the slope value of this peak, the propagation velocity of flow structures, U_v, can be calculated as:

$$U_v = \frac{2\pi f}{k_v} = 2\pi \cdot 3.48\ m/s \approx 21.88\ m/s \approx 0.57 \cdot U_\infty \quad (9)$$

That is, κ in Eq. (1) is approximately equal to 0.57 for the base cavity configuration, when the Ma number is 0.11.

Figure 15 shows the wavenumber-frequency spectral analysis results for all cases except the Base case, focusing on the slopes of the peaks associated with fluid wave propagation. As in Fig. 14, multiple peaks with concentrated energy are observed in Fig. 15 (a) to Fig. 15 (e). These peaks correspond to the characteristic frequencies of the main modes, flow structure motion, and acoustic wave propagation, respectively. The left image in Fig. 15 (f) shows that the slope of the peak corresponding to fluid wave propagation decreases as the cavity depth increases. The right image in Fig. 15 (f) displays the slope values of these peaks along with the corresponding propagation velocities of the flow structures, U_v. It is evident that both the slope and the propagation velocity of the flow structures linearly decrease with increasing cavity depth.

Fig. 16 shows the numerical simulation results of the frequencies and the results predicted using Rossiter's empirical formula. The white dashed lines are the results of the empirical formula prediction, where $\alpha = 0.58e^{-((L/D-10)/6)^2}$ and κ is determined by the wavenumber-frequency spectral method. The predicted characteristic frequencies, indicated by the white dashed lines, align well with the calculated results for most noise characteristic frequencies, excluding the 3rd modal noise. Notably, the predictions closely match the calculated results for cavity depths of 0.14 m and 0.16 m. However, for depths of 0.1 m and 0.12 m, the deviation between the prediction and calculation is approximately 100 Hz, the largest deviation observed. As the depth decreases further, the deviation from the prediction decreases to less than 50 Hz.

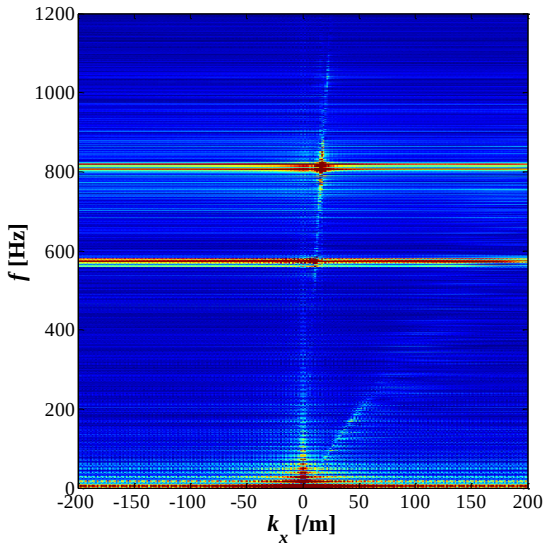

(a) Case1

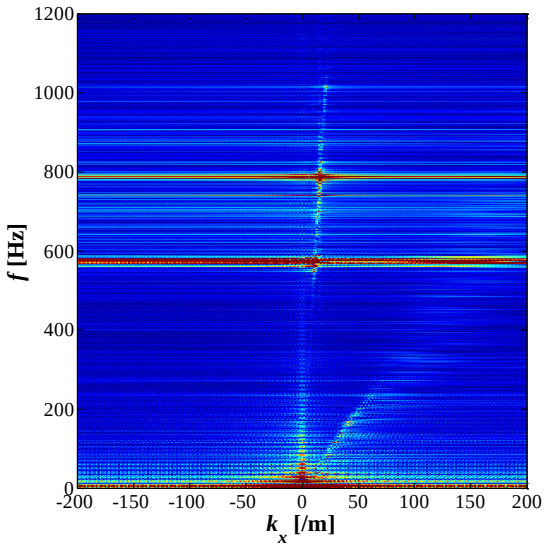

(b) Case2

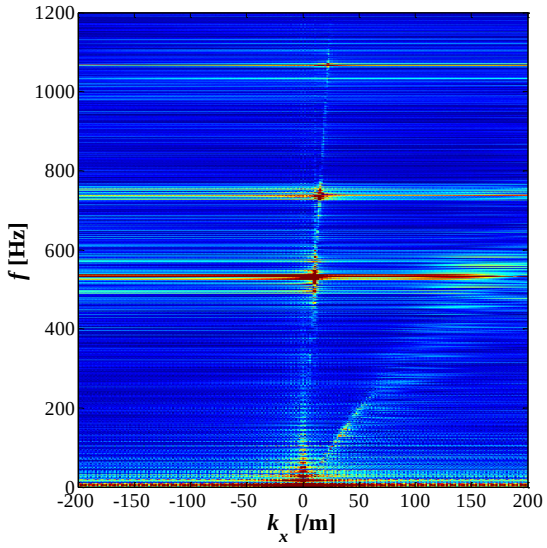

(c) Case3

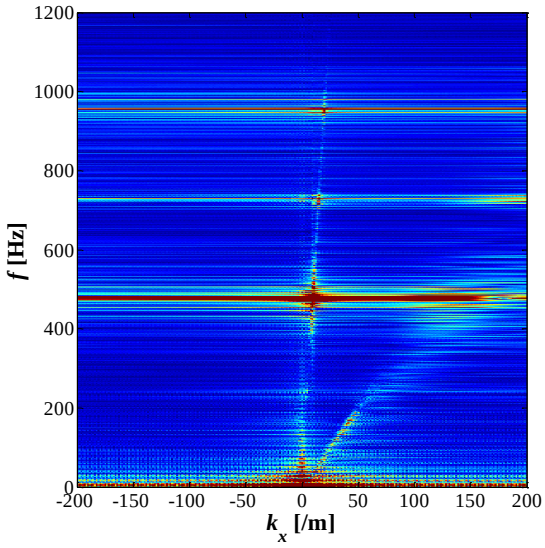

(d) Case4

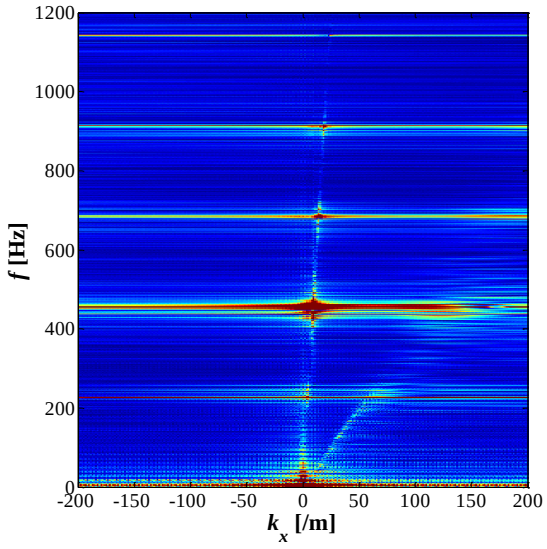

(e) Case5

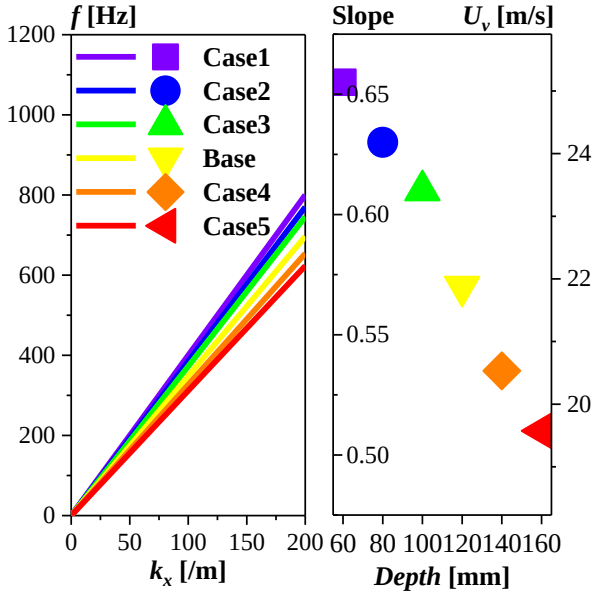

(f) Slopes and U_v

Fig. 15 Wavenumber-frequency spectral diagram and the slopes of the peaks corresponding to fluid wave propagation

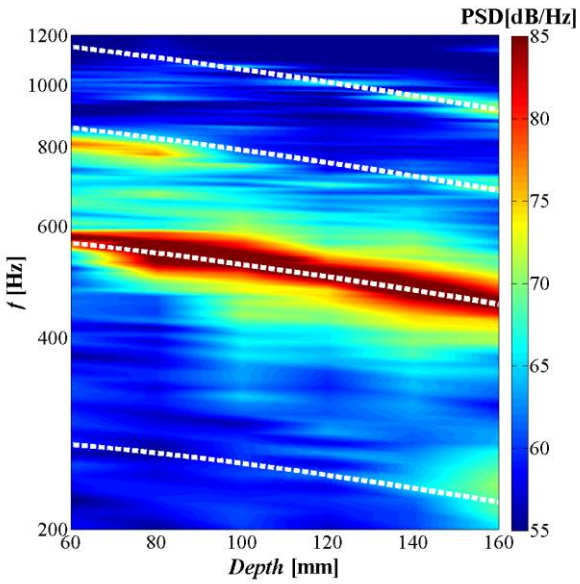

Fig. 16 Comparison of results from numerical simulation and empirical prediction of the far-field noise at Ma=0.11

5. CONCLUSION

This paper explored the flow characteristics of the boundary/shear layer near cavity mouths and the flow-acoustic feedback noise characteristics in cavities with different depths but identical lengths. The cavities investigated in this study had length-to-depth ratios ranging from 1/2 to 4/3. The first objective was to elucidate the convective characteristics of the shear layer in low aspect ratio cavities at low speeds. The second objective was to predict the characteristic frequencies of the flow-acoustic feedback noise using the wavenumber-frequency spectral method and Rossiter's empirical formula. The findings can be summarized as follows:

(1) For cavities with low aspect ratios of 1/2 to 4/3, multiple narrowband noises within a frequency range of 0.2 kHz to 2 kHz were observed. These were attributed to flow-acoustic feedback phenomena. Notably, as the cavity depth increased, the characteristic frequencies associated with a given mode of flow-acoustic feedback noise consistently shifted linearly toward lower frequency bands.

(2) Examination of the flow field characteristics, specifically the time-averaged velocity and velocity fluctuation near the cavity mouth, demonstrated increases along the development direction of the shear layer. Furthermore, the cavity depth influenced the velocity fluctuation significantly, with deeper cavities associated with larger changes in velocity fluctuation and smaller time-averaged velocities.

(3) A wavenumber-frequency spectral analysis of flow field information revealed the presence of multiple energy-concentrated peaks. These corresponded to the characteristic frequencies of the main modes, fluid wave propagation, and acoustic-wave propagation. The propagation direction and velocity of the flow structures, represented by U_v , were determined through this analysis. Incorporating U_v into Rossiter's empirical formula showed that predicted characteristic frequencies aligned well with calculated results.

The combined utilization of the wavenumber-frequency analysis method and Rossiter's empirical formula proved effective in accurately predicting the characteristic frequencies of flow-acoustic feedback noise generated by low aspect ratio cavities. Additionally, this approach enabled the quantification of the time-averaged convection velocity of the shear layer near the cavity mouth.

ACKNOWLEDGEMENTS

This work was supported by National Key Research and Development Program (Grant No. 2022YFB2603400) and Postdoctoral Fund of Chinese Academy of Sciences (Grant No. E2XM0404).

CONFLICT OF INTEREST

There is no conflict of interest.

AUTHORS CONTRIBUTION

Conceptualization, **W. Lu**, **G. Zheng** and **G. Yang**; formal analysis **W. Lu**; writing—original draft preparation, **W. Lu**; writing—review and editing, **Y. Wang** and **Z. Sun**. All authors have read and agreed to the published version of the manuscript.

REFERENCES

Ahuja, K., & Mendoza, J. (1995). *Effects of cavity dimensions, boundary layer, and temperature in cavity noise with emphasis on benchmark data to validate computational aeroacoustic codes.* United States: NASA CR-4653. https://ntrs.nasa.gov/citations/19950018459

Arguillat, B., Ricot, D., Robert, G., & Bailly, C. (2005). *Measurements of the wavenumber-frequency spectrum of wall pressure fluctuations under turbulent flows.* 11th AIAA/CEAS Aeroacoustics Conference. Monterey, California, AIAA paper 2005-2855. https://arc.aiaa.org/doi/abs/10.2514/6.2005-2855

Ashcroft, G., & Zhang, X. (2001). *A computational investigation of the noise radiated by flow-induced cavity oscillations.* 39th Aerospace Sciences Meeting and Exhibit. Reno, NV, U.S.A., AIAA paper 2001-512. https://arc.aiaa.org/doi/abs/10.2514/6.2001-512

Bremner, P. G., & Zhu, M. (2003). *Recent progress using sea and cfd to predict interior wind noise*. SAE transactions 2003-01-1705. https://doi.org/10.4271/2003-01-1705

Casalino, D., Gonzalez-Martino, I., & Mancini, S. (2022). On the rossiter-heller frequency of resonant cavities. *Aerospace Science and Technology, 131*(2022), 108013. https://doi.org/10.1016/j.ast.2022.108013

Casalino, D., Ribeiro, A. F. P., & Fares, E. (2014). Facing rim cavities fluctuation modes. *Journal of Sound & Vibration*, *333*(13), 2812-2830. https://doi.org/10.1016/j.jsv.2014.01.028

Chen, G.Y., Tang, X. L., Yang, X. Q., Weng, P.F, & Ding, J. (2021). Noise control for high-lift devices by slat wall treatment. *Aerospace Science and Technology*, *115*(2021), 106820. https://doi.org/10.1016/j.ast.2021.106820

Comte, P., Daude, F., & Mary, I. (2008). Simulation of the reduction of unsteadiness in a passively controlled transonic cavity flow. *Journal of Fluids and Structure*, *24*(8), 1252-1261. https://doi.org/10.1016/j.jfluidstructs.2008.08.001

Dalmont, J. P., Nederveen, C. J., & Joly, N. (2001). Radiation impedance of tubes with different flanges: numerical and experimental investigations. *Journal of Sound and Vibration*, *244*, 505–534. https://doi.org/10.1006/jsvi.2000.3487

DeChant, L. (2019). A cavity depth sensitized Rossiter mode formula. *Applied Mathematics and Computation*, *347*(2019), 143-148. https://doi.org/10.1016/j.amc.2018.10.048

Delcor, L., Parizet, E., & Ganivet-Ouzeneau, J., & Caillet, J (2022). Model of sound and vibration discomfort in helicopter cabins. *Applied Acoustics*, *195* (2022), 108847. https://doi.org/10.1016/j.apacoust.2022.108847

Dobrzynski, W. (2010). Almost 40 years of airframe noise research: What did we achieve? *Journal of Aircraft*, *47*, 353–67. https://doi.org/10.2514/1.44457.

East, L. F. (1966). Aerodynamically induced resonance in rectangular cavities. *Journal of Sound and Vibration*, *3*(3), 277-287. https://doi.org/10.1016/0022-460X(66)90096-4

Ffowcs-Williams, J. E., & Hawkings, D. L. (1969). Sound generation by turbulence and surfaces in arbitrary motion. *Philosophical Transactions of the Royal Society of London. Series A, Mathematical and Physical Sciences*, *264* 321 – 342. https://doi.org/10.1098/rsta.1969.0031

Forestier, N. (2000). *Etude experimentale d'une couche cisaillee au-dessus d'une Cavite en regime transsonique*. France: Ecole Centrale de Lyon (in French). https://doi.org/10.1007/BF00122093

Gharib, M., & Roshko, A. (1987). The effect of flow oscillation on cavity drag. *Journal of Fluid and Mechanics*, *177*, 501-530. https://doi.org/10.1017/S002211208700106X

Guo, R., Chen, X., Wan, Z., Hu, H., & Cui, S. (2022). Noise reduction in cavity flow by addition of porous media. *Acta Mechanica Sinica 38*, 321358. https://doi.org/10.1007/s10409-021-09043-x

Guo, Z. (2020). *Investigation on aeroacoustic noise mechanism and noise control methods of cavity structure in landing gear*. China: Beihang University. (in Chinese).

Guo, Z., Liu, P., & Guo, H. (2021). Control effect on deep cavity noise by slanted walls at low Mach numbers. *Journal of Vibration and Control*, *27*(9-10), 998-1008. https://doi.org/10.1177/1077546320936510

Heller, H. H., Holmes, D. G., & Covert, E. E. (1971). Flow induced pressure oscillations in shallow cavities. *Journal of Sound and Vibration 18* (4), 545–553. https://doi.org/10.1016/0022-460X(71)90105-2

Ji, M., & Wang, M. (2012). Surface pressure fluctuations on steps immersed in turbulent boundary layers. *Journal of Fluid and Mechanics*, *7*(12), 471-504. https://doi.org/10.1017/jfm.2012.433

Larcheveque, L., Pierre, S., Ivan, M., Labbe, O & Comte, P. (2003). Large-eddy simulation of a compressible flow past a deep cavity. *Physics of Fluids*, *15*, 193. https://doi.org/10.1017/jfm.2012.433

Li, W., Nonomura, T., & Fujii, K. (2013). On the feedback mechanism in supersonic cavity flows. *Physics of Fluids*, *25*, 056101. https://doi.org/10.1063/1.4804386

Ma, R., Slaboch, P. E., & Morris, S. C. (2009). Fluid mechanics of the flow-excited Helmholtz resonator. *Journal of Fluid Mechanics*, *2009*(623), 1-26. https://doi.org/10.1017/S0022112008003911

Menter, F. R. (1994). Two-equation eddy-viscosity turbulence models for engineering applications. *AIAA Journal*, *32*(8), 1598–1605. https://doi.org/10.2514/3.12149

Moreau, S. (2022). The third golden age of aeroacoustics. *Physics of Fluids*, *34*(3), 031301. https://doi.org/10.1063/5.0084060

Powell, A. (1961). On the edgetone. *The Journal of the Acoustical Society of America*, *33*(4), 395–409. https://doi.org/10.1121/1.1908677

Rockwell, D., & Naudascher, E. (1978). Review: Self-sustaining Oscillations of flow past cavities. *Journal of Fluids Engineering, Transactions of the ASME*. *100* (2), 152-165. https://doi.org/10.1115/1.3448624

Roshko, A. (1955). *Some measurements of flow in a rectangular cutout*. California: NACA-TN-3488. https://digital.library.unt.edu/ark:/67531/metadc57850/

Rossiter, J. E. (1964). *Wind-Tunnel Experiments on the Flow over Rectangular Cavities at Subsonic and Transonic Speeds*. Netherlands: Ministry of Aviation, Royal Aircraft Establishment; RAE Memoranda, RAE Technical Report: 64037. https://reports.aerade.cranfield.ac.uk/handle/1826.2/4020

Shur, M. L., Spalart, P. R., Strelets, M. K., & Travin, A. K. (2008). A hybrid RANS-LES approach with delayed-DES and wall-modelled LES capabilities. *International Journal of Heat and Fluid Flow*, *29*(6), 1638-1649. https://doi.org/10.1016/j.ijheatfluidflow.2008.07.00

1

Spalart, P. R. (1997). *Comments on the feasibility of LES for wings, and on a hybrid RANS/LES approach.* Advances in DNS/LES, Greyden Press, Columbus, OH, USA.

Spalart, P. R., Deck, S., Shur, M. L., Squires, K. D., Strelets, M. K., & Travin, A. (2006). A new version of detached-eddy simulation, resistant to ambiguous grid densities. *Theoretical and Computational Fluid Dynamics*, *20*(3), 181-195. https://doi.org/10.1007/s00162-006-0015-0

Tang, Y. P., & Rockwell, D. (1983). Instantaneous pressure fields at a corner associated with vortex impingement. *Journal of Fluid and Mechanics*, *126*, 187–204. https://doi.org/10.1017/S0022112083000105

Vadsola, M., Agbaglah, G. G., & Mavriplis, C. (2021). Slat cove dynamics of low Reynolds number flow past a 30P30N high lift configuration. *Physics of Fluids*, *33*(3), 033607. https://doi.org/10.1063/5.0036088

Zhang, M., & Filippone, A. (2022). Optimum problems in environmental emissions of aircraft arrivals. *Aerospace Science and Technology*, *123*(2022),107502. https://doi.org/10.1016/j.ast.2022.107502

Zhao, K., Okolo, P., Neri, E., Chen, P., Kennedy, J., & Bennett, G. J. (2020). Noise reduction technologies for aircraft landing gear-A bibliographic review. *Progress in Aerospace Sciences*, *112*, 100589. https://doi.org/10.1016/j.paerosci.2019.100589